Check for updates

High Power Laser Science and Engineering, (2026), Vol. 14, e15, 10 pages.
doi:10.1017/hpl.2025.10105

HIGH POWER LASER SCIENCE AND ENGINEERING

RESEARCH ARTICLE

Efficient plasma-based polarization converter for intense X-ray lasers

Yijie Dong, Taiwu Huang, Peng Chen, Ke Jiang, Hao Peng, Ran Li, Mingyang Yu, and Cangtao Zhou

Shenzhen Key Laboratory of Ultraintense Laser and Advanced Material Technology, Center for Intense Laser Application Technology, and College of Engineering Physics, Shenzhen Technology University, Shenzhen, China

(Received 8 September 2025; revised 13 November 2025; accepted 24 December 2025)

Abstract

Precise control of the polarization of X-ray lasers is crucial in broad applications such as ultrafast-physics experiments and material characterization. Existing X-ray polarization converters, however, are mainly suited for low-power conditions and usually suffer from either large size or low conversion efficiency. Here we propose a compact and efficient scheme for polarization conversion of high-power, high-intensity femtosecond X-ray lasers, based on linear total internal reflection at the interface of the vacuum and solid-density plasma plate. Particle-in-cell simulations show that although the reflectivity is affected by the density oscillations of the surface plasma waves that are inevitably excited, the single-pass reflectivity can still exceed 95% and approach 100% for a broad range of laser parameters. Beyond its high conversion efficiency and damage resistance, this method offers dynamic tunability and enables ultrafast polarization switching (sub-ps), positioning it as a compact and innovative solution for polarization control in high-power X-ray laser systems.

Keywords: high-power X-ray laser; polarization state conversion; solid-density plasma plate; total internal reflection

1. Introduction

X-ray lasers are useful for probing the internal structures of complex materials and the dynamics of microscopic processes, such as in materials characterization[1–4] and biomolecular imaging[5–7]. In particular, high-intensity X-ray lasers can also be used to drive chip-size particle acceleration and explore vacuum birefringence physics[8,9]. As a fundamental optical property in light–matter interaction, precise and/or tunable control of the polarization is often essential[10–12]. However, existing X-ray polarization converters usually operate for low-power conditions with characteristic trade-offs. For example, undulator-based systems (e.g., delta/elliptical undulators in the soft X-ray free-electron laser, SXFEL) achieve high polarization[13,14] with femtosecond pulse capability and two-color operation, but are constrained to soft X-rays, large footprints (>10 m) and slow switching ($\sim$ms). Diamond X-ray phase retarders (XPRs) offer compact design and can realize circular polarization through birefringence modulation with sub-ms switching, yet suffer from low conversion efficiency and discrete tuning[15].

Recent advances in X-ray lasers have seen dramatic increases in both intensity and power. Multiple approaches have been proposed to generate multiterawatt (TW) X-ray pulses at X-ray free-electron laser (XFEL) facilities[16–18], including high-order-harmonic generation (HHG) from laser–solid interactions, which has demonstrated the potential to produce isolated 100-TW X-ray pulses[19]. In addition, recently proposed X-ray laser focusing schemes[20,21] show promise for generating relativistic-intensity X-ray outputs. To date, hard X-ray (i.e., very short wavelength) XFELs can be focused to a 7 nm spot at $10^{22}\,\mathrm{W/cm^2}$ intensity[22]. The dramatic increase in X-ray power and intensity makes conventional polarizers (e.g., undulators, diamond XPRs) more prone to damage, necessitating significantly enhanced damage resistance in polarization optics. To avoid optical damage by high-power, high-intensity lasers in applications, plasma-based components such as plasma mirrors[23–25], plasma refractors[26], plasma lenses[27,28], plasma switches[29] and plasma amplifiers[30,31] have been proposed. These plasma devices themselves are resistant to optical damage, providing a promising alternative to address the problem of polarization control of high-power X-ray lasers.

In this paper, we propose using a solid-density plasma plate for tailoring the polarization of ultrashort, high-power and high-intensity X-ray laser pulses. Since the refractive index of the solid-density plasma for X-ray lasers is less

Correspondence to: T. Huang, College of Engineering Physics, Shenzhen Technology University, Shenzhen 518118, China. Email: taiwu.huang@sztu.edu.cn

© The Author(s), 2026. Published by Cambridge University Press in association with Chinese Laser Press. This is an Open Access article, distributed under the terms of the Creative Commons Attribution licence (https://creativecommons.org/licenses/by/4.0), which permits unrestricted re-use, distribution and reproduction, provided the original article is properly cited.

https://doi.org/10.1017/hpl.2025.10105 Published online by Cambridge University Press

than unity, the vacuum–plasma interface can serve as a total internal reflection (TIR) surface[32]. Laser light incident on the plasma surface at a greater angle than the critical angle θ_c will be totally reflected. As the reflection is accompanied by phase and polarization shifts of the light, by tailoring the laser wavelength, angle of incidence and/or plasma electron density, one can achieve continuous tuning of its polarization, including linear, elliptical and circular polarization, and this tuning process is linear. We analytically estimate and particle-in-cell simulate tailored mode conversion of short-pulse X-ray laser light using solid-density plasmas. It is found that for $10^{18}-10^{22}$ W/cm^2 (or $0.01-1$ TW) femtosecond X-ray laser pulses, over 95% and nearly 100% efficiency of X-ray polarization conversion is possible. Moreover, this method potentially offers distinct advantages: compact size, high conversion efficiency, ultrafast polarization modulation (sub-ps) and no damage threshold – making it a reliable solution for demanding applications in high-power X-ray laser systems.

2. Model analysis

Figure 1 shows the X-ray polarization converter based on linear TIR. The X-ray laser pulse is obliquely incident on the surface of a solid-density plasma with a refractive index less than unity. TIR occurs[32,33] if the incident angle θ_i exceeds the critical angle $\theta_c = \arcsin(n_2/n_1) = \arcsin(n_p)$, where $n_1 = 1$ and $n_2 = n_p < 1$ are the refractive indices of the vacuum and plasma, respectively. This process is governed by the Fresnel equations, which describe the amplitude and phase relationships of the reflected and transmitted waves at interfaces. Under the boundary continuity condition (i.e., matching of electromagnetic field components at the interface), TIR induces not only incident and reflected waves but also evanescent waves penetrating the plasma medium. This surface wave acts as an energy buffer, temporarily storing and redistributing energy flux to maintain conservation during the TIR[34]. The x and y components of the laser's Poynting vector of the surface wave are as follows:

$$S_{Px} = -\frac{k_t}{2w}\left(\frac{\sin\theta_i}{n_p}\right)D_0^2\left(1+\cos\left(2\left(k_t\frac{\sin\theta_i}{n_p}x-\omega t\right)\right)\right), \tag{1}$$

$$S_{Py} = \frac{k_t}{2w}\sqrt{\frac{\sin^2\theta_i}{n_p^2}-1}\,D_0^2\sin 2\left(k_t\frac{\sin\theta_i}{n_p}x-\omega t\right), \tag{2}$$

$$D_0 = e_z E_0^t \exp\left(-k_t\left(\frac{\sin^2\theta_i}{n_p^2}-1\right)^{\frac{1}{2}}y\right), \tag{3}$$

where k_t is the wave vector in the x-direction, ω denotes the laser angular frequency and E_0^t represents the electric field amplitude of the refracted light. Within half a laser period, the energy of the surface wave enters the plasma and is stored in a thin layer near the interface. In the other half of the period, this energy is released and becomes the energy of the reflected wave. However, the average value is zero within the same period. Therefore, during TIR, the instantaneous energy flow in the direction perpendicular to the interface within the penetration depth is not zero, but the average energy flow is zero. That is, the conversion from incident to reflected waves is mediated by the surface wave's energy oscillation, leading to a phase shift in the reflected polarization states.

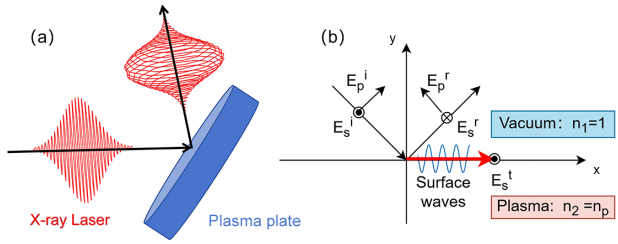


Figure 1. (a) Schematic of the proposed scheme. (b) Total internal reflection at the plasma surface. Here, E denotes the electric field, while the superscripts i, t and r denote the incident, refracted and reflected light, respectively. The subscripts s and p denote the s- and p-polarization components of the laser.

In linear TIR, we have $\sin\theta_i > n_p$, $\cos\theta_t = i\sqrt{\sin^2\theta_i/n_p^2-1}$, where θ_i and θ_t represent the incident and refracted angles, respectively. By substituting the Fresnel equations and performing algebraic manipulations, the following relations can be readily obtained[35]:

$$\frac{E_s^r}{E_s^i} = e^{-i\delta_s}, \quad \tan\frac{\delta_s}{2} = \frac{\sqrt{\sin^2\theta_i-n_p^2}}{\cos\theta_i}, \tag{4}$$

$$\frac{E_p^r}{E_p^i} = e^{-i\delta_p}, \quad \tan\frac{\delta_p}{2} = \frac{\sqrt{\sin^2\theta_i-n_p^2}}{n_p^2\cos\theta_i}, \tag{5}$$

where E_s^i, E_p^i, E_s^r and E_p^r are the electric field amplitudes of the s-polarized (perpendicular to the incident plane) and p-polarized (parallel to the incident plane) components of the incident and reflected light, respectively. It can be seen that the electric field magnitudes of the p- and s-polarized components of the reflected light are the same as that of the incident laser, or $|E_s^r| = |E_s^i|$, $|E_p^r| = |E_p^i|$. However, both undergo phase shifts δ_s and δ_p relative to incident light, and the phase difference $\delta = \delta_p - \delta_s$ is given by the following:

$$\tan\left(\frac{\delta}{2}\right) = \tan\left(\frac{\delta_p-\delta_s}{2}\right) = \frac{\cos(\theta_i)\sqrt{\sin^2(\theta_i)-(n_p)^2}}{\sin^2(\theta_i)}. \tag{6}$$

In this model, the X-ray laser propagates in a vacuum and undergoes TIR at the plasma surface, enabling conversion

https://doi.org/10.1017/hpl.2025.10105 Published online by Cambridge University Press

of the polarization state. For X-rays, the refractive index in the solid-density plasma is given by $n_p = \sqrt{1 - n_e/n_c}$. For a relatively short-wavelength X-ray laser, $n_e < n_c$ and $n_p < 1$, where n_e denotes the electron density, and the critical density n_c is given by $n_c = m_e\omega_0^2/4\pi e^2 = n_0/\lambda_{nm}^2$. Here, m_e is the electron mass, ω_0 is the central angular frequency and e is the elementary charge. The parameter $n_0 \approx 1.1 \times 10^{33}$ m^{-3}, and λ_{nm} is the laser wavelength normalized to nanometers (nm). Letting $\alpha \equiv \tan\left(\frac{\delta}{2}\right)$ and substituting the expression of n_p in Equation (6), we get the following:

$$\lambda_{nm} = \sqrt{\frac{n_0}{n_e}} \times \sqrt{1 - \sin^2\theta_i\left(1 - \alpha^2\tan^2\theta_i\right)}. \tag{7}$$

This equation describes the relation among the laser wavelength, the incident angle and the phase shift. The value of δ can range from 0 to $\pi/2$, so that $0 < \alpha \leq 1$, where $\alpha = 1$ refers to the conversion from linear to circular polarization. Equation (7) suggests an upper limit of the laser wavelength as $\lambda_{nm} < \sqrt{\frac{n_0}{n_e}}$, which corresponds to the condition of $n_e < n_c$. For example, for a solid-density Al plasma with $n_e = 7.8 \times 10^{29}$ m^{-3}, this gives an upper limit of 37.5 nm. Namely, for an X-ray laser with $\lambda_{nm} < 37.5$ nm, conversion from linear to elliptic (including circular) polarization can be achieved.

It is interesting to note that for oblique incidence, the effective critical density for laser reflection is reduced by $n_c' = n_c\cos\theta^2$, where θ is the incident angle[36]. This indicates that laser reflection could occur for $n_e > n_c'$. For the case of TIR, the critical angle for TIR can be written as $\theta_c = \arcsin\left(\sqrt{1 - \frac{n_e}{n_c}}\right)$. That is, the critical angle corresponds to $n_e = n_c\cos\theta_c^2 = n_c'$. When the incident angle θ exceeds the critical angle θ_c, TIR occurs. This actually also corresponds to the condition of $n_e > n_c'$. Thus, these two descriptions actually are equivalent.

3. Particle-in-cell simulations

To verify the above scheme, we have performed a two-dimensional (2D) PIC simulation using EPOCH code[37]. Firstly, we demonstrated the feasibility of polarization state conversion, where linearly polarized (LP) X-ray laser pulses can be converted into circularly polarized (CP) or elliptically polarized (EP) laser pulses. The LP X-ray laser pulse is of incident angle $\theta_i = 41.3°$ (far exceeding the critical angle of about 18.4° for the parameters given here), wavelength of $\lambda_0 = 36$ nm, (full width at half-maximum) duration of $\tau = 2.12$ fs and radius of $5.6\lambda_0$. The incident light is initially LP and consists of both p-polarized and s-polarized components with identical phase and amplitude. The laser intensity is $I = 8 \times 10^{18}$ W/cm^2, so that relativistic amplitude of laser $a_0 = eE_0/m_e\omega_0 c = 0.087$, where E_0 is the laser amplitude

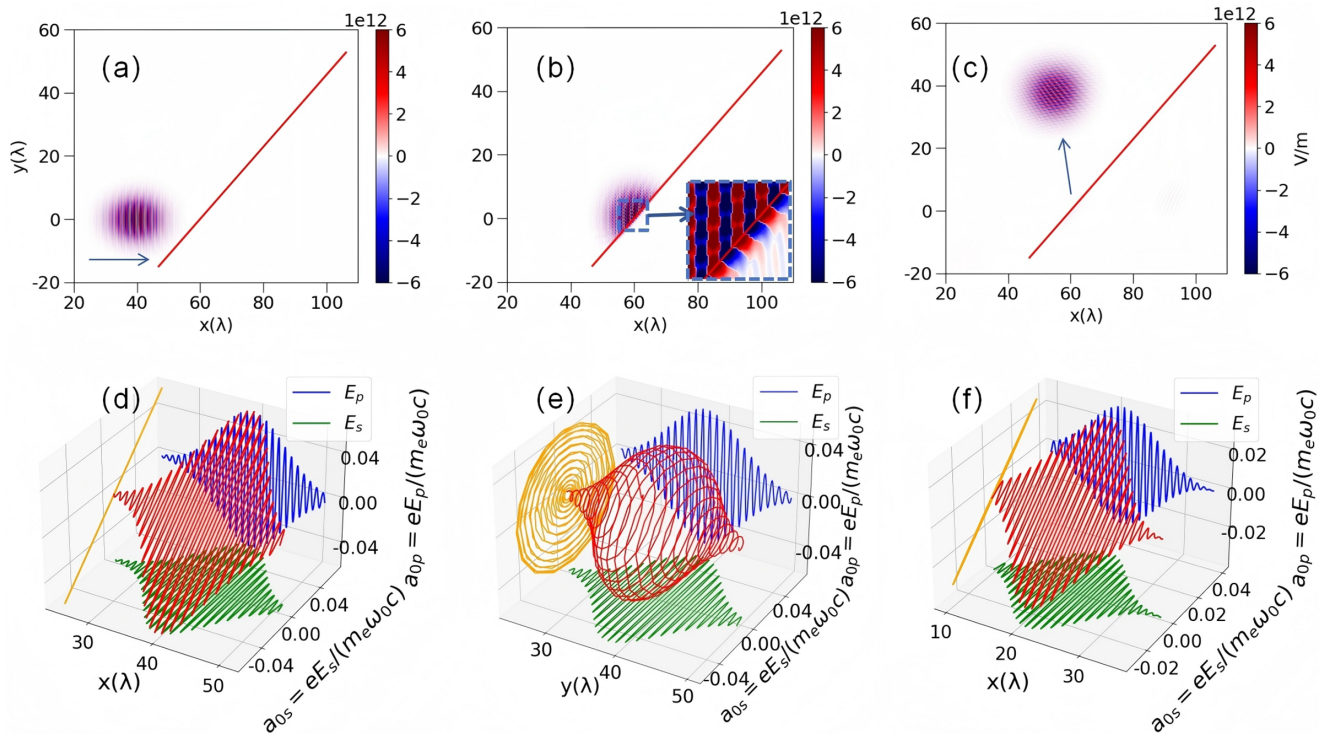


Figure 2. Electric field distributions in the laser–plasma interaction. Electric field of the incident laser pulse at (a) $t = 60T_0$ and (b) at $t = 82T_0$, as it reaches the surface. (c) Electric field distribution of the circularly polarized reflected wave at $t = 120T_0$. Electric field on the laser axis of (d) the incident laser and (e) the reflected pulse. In the above, the laser incidence angle is 41.3°. (f) Electric field of the reflected pulse for 0° incidence angle. In all the lower panels, the 3D field vector (red), profiles of the two orthogonal field components E_s (green) and E_p (blue) and the projection of $E_s - E_p$ (orange) are displayed.

https://doi.org/10.1017/hpl.2025.10105 Published online by Cambridge University Press

and c is the speed of light in vacuum. The laser pulse is focused on the target, which is a fully ionized solid aluminum plasma slab of electron density $n_e = 7.8 \times 10^{29}\,\mathrm{m}^{-3}$, or approximately $0.9n_c$. The initial temperature of the electrons is 1 keV. Such plasma can be experimentally generated by using a double-laser irradiation scheme[38], which has led to very homogeneous, micrometer-scale, solid-density plasma with a well-defined structure and temperature ranging from 0.25 to 2.5 keV. In this case, the assumption of an ideal plasma is applicable, and the ionization effect of the X-ray laser can also be neglected.

The simulation domain extends from 0 to $120\lambda_0$ in the x-direction and from $-20\lambda_0$ to $100\lambda_0$ in the y-direction. The simulation uses an ultra-high-resolution 2D grid configuration with 7680×7680 grid points, a grid spacing of $\lambda_0/64$ (corresponding to 64 points per wavelength) and a high-density particle distribution (10 particles per grid point). The surface wave skin depth is $l_{\mathrm{skin}} = \lambda_0 / \left(2\pi n_p \sqrt{\sin^2\theta_i / n_p^2 - 1}\right) \approx 0.94\lambda_0$. The resolution of the simulation is thus much smaller than l_{skin}, ensuring that the physical processes in the plasma boundary layer are adequately resolved.

Figure 2(a) shows the electric field distribution of the incident X-ray laser, and Figure 2(b) shows the electric field distribution at the moment of laser–plasma interaction. It can be observed that surface waves moving along the interface exist within the plasma medium. Figure 2(c) shows the electric field distribution of the reflected X-rays. The reflectivity reaches 99.97%, indicating that almost all incident light is reflected. This high reflectivity not only verifies the effectiveness of the polarization conversion mechanism based on TIR, but also holds significant implications for practical applications.

The LP incident laser waveform, as illustrated in Figure 2(d), exhibits an electric field comprising two orthogonal components (p- and s-components) E_p^i and E_s^i with identical amplitudes and phases $\phi_p^i = \phi_s^i$. Figure 2(e) displays the reflected laser electric field from the target surface, showing that the polarization state has been converted into left-handed circular polarization with Stokes parameter $P = -0.95 \pm 0.05$. The closer the absolute value of P is to 1, the higher the degree of circular polarization. Specifically, $P > 0$ indicates right-handed circular polarization, while $P < 0$ indicates left-handed circular polarization. Due to the TIR effect induced by oblique incidence, the phase difference between the reflected field components E_p^r and E_s^r shifts from 0 to $\pi/2$ approximately. To further verify this phenomenon, Figure 2(f) shows the reflected laser electric field under normal incidence ($\theta = 0°$). Since TIR did not occur, the laser undergoes refraction and reflection at the interface, resulting in the reflected optical electric field being much smaller than the incident optical electric field, and the polarization state of the reflected laser pulse remains linear.

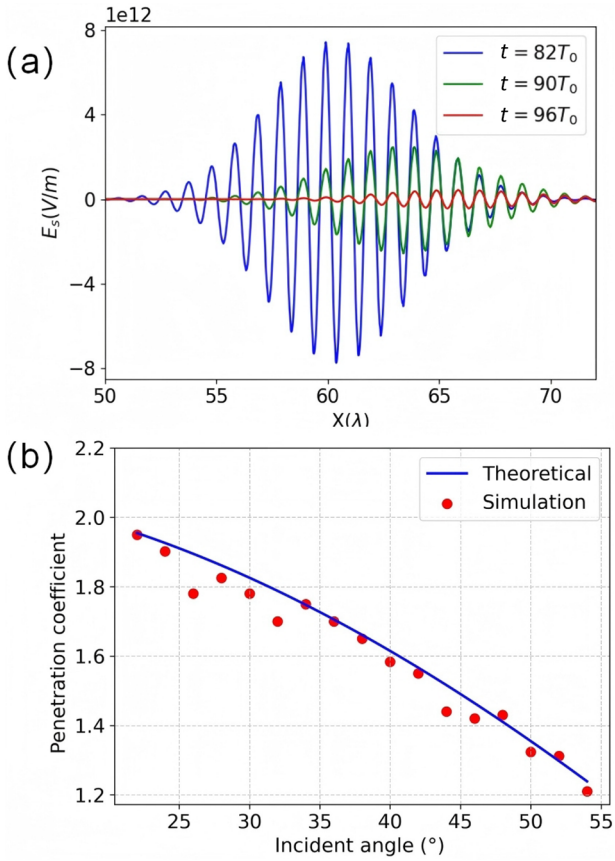


Figure 3. (a) The s-polarized electric field of the surface wave E_s^t at different moments. (b) The transmission coefficient of E_s^t at different incident angles.

When the incident angle exceeds the critical angle for TIR, the refracted wave is converted into a surface wave. This surface wave then ultimately transforms into the reflected wave, and it is precisely this conversion sequence that gives rise to the change in the phase difference of the reflected wave. To visualize this dynamic process, Figure 3(a), derived from 2D PIC simulations, illustrates the s-component electric field of the surface wave E_s^t at various instants. When $t = 82T_0$, where T_0 represents the characteristic period of the incident laser, the moment of interaction between the laser and the plasma surface occurs. At this juncture, E_s^t reaches its maximum value. As time progresses, it is evident that the amplitude of the surface wave gradually diminishes, and during this period, the surface wave undergoes a gradual transformation into the reflected wave, completing the TIR process.

Figure 3(b) shows the transmission coefficients of E_s^t under different incident angles. As the incident angle increases, the electric field amplitude of the surface wave gradually weakens, and this phenomenon is consistent with the following theoretical formula:

$$|t_s| = \left|\frac{E_s^t}{E_s^r}\right| = \frac{2\cos\theta_i}{\sqrt{1-n_p^2}}, \tag{8}$$

https://doi.org/10.1017/hpl.2025.10105 Published online by Cambridge University Press

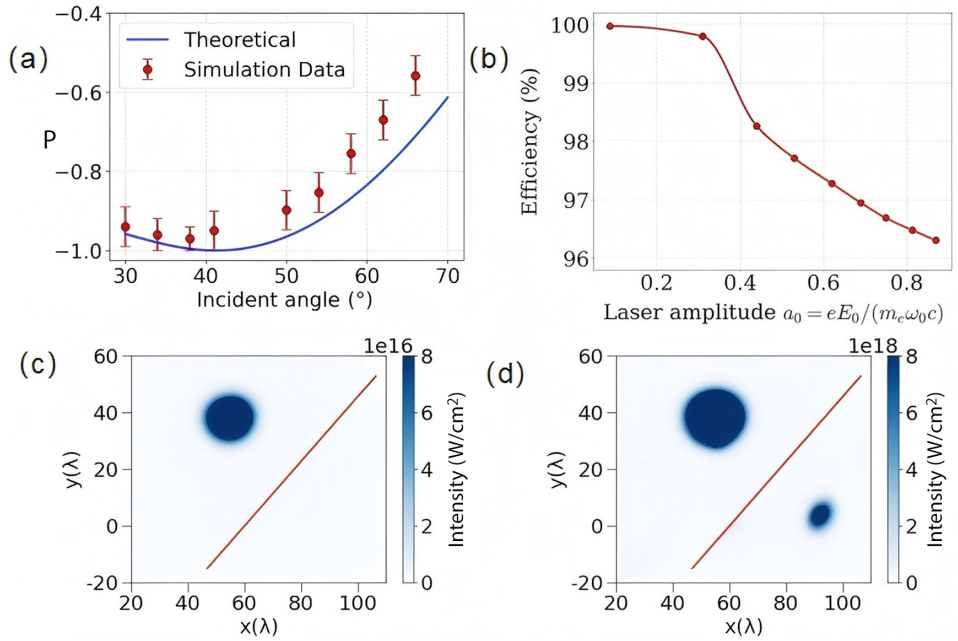


Figure 4. (a) The Stokes parameter P under different incident angles. (b) Reflection efficiencies for different normalized laser amplitudes a_0. (c) The laser intensity distribution of the reflected wave when the normalized laser amplitude $a_0 = 0.087$. (d) The laser intensity distribution of the reflected wave when the normalized laser amplitude $a_0 = 0.87$. To display the distribution of the transmitted laser, the magnitude of the colorbar is reduced by two orders of magnitude.

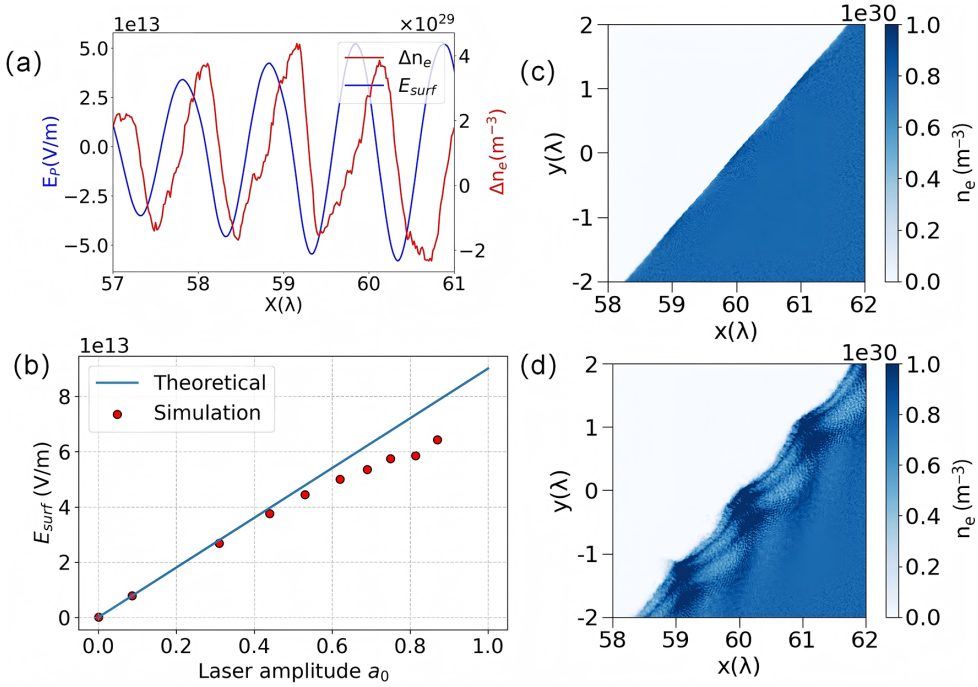


Figure 5. (a) Electron density and electric field variation at the interface for $a_0 = 0.87$. (b) Electric field of surface wave versus a_0. (c) Electron density distribution for $a_0 = 0.087$. (d) Electron density distribution for $a_0 = 0.87$.

where t_s is the transmission coefficient and E_s^t and E_s^r represent the electric fields of the surface wave (transmitted wave) and the reflected wave, respectively. This formula, grounded in the fundamental principles of electromagnetic wave propagation at the plasma–vacuum interface, provides a theoretical framework for predicting the behavior of surface waves. The close match between the simulation results and the theoretical formula, as shown in Figure 3(b), further validates the accuracy of our theoretical model.

Next we demonstrate that this plasma-based polarization modulator is tunable and capable of achieving a controllable phase shift between two orthogonal field components.

https://doi.org/10.1017/hpl.2025.10105 Published online by Cambridge University Press

Specifically, in TIR process, the phase difference between p- and s-polarized components varies with the incident angle, as indicated in Equation (6), which endows this principle with continuous tunability. Figure 4(a) shows the simulation and theoretical results of the Stokes parameter of the reflected laser under different incident angles. It can be seen that the simulation results agree well with the theoretical results, and demonstrate the tunability of the polarization degree in the present scheme.

We further consider the influence of laser amplitude a_0. The normalized amplitude $a_0 = eE/m_e\omega c$, as a core Lorentz invariant, holds the following physical significance: when $a_0 \geq 1$, the laser intensity enters the fully relativistic regime. In the near-threshold region ($0.1 < a_0 < 1$), the plasma target structure can already be modified through the density perturbation mechanism (see Figure 5(d)). As shown in Figure 4(b), although the overall conversion efficiency gradually decreases with increasing a_0, it remains above 95% across the studied intensity range. Furthermore, we verified that even under specific extreme parameters with a wavelength of 10 nm and a laser intensity of 10^{22} W/cm^2 (the corresponding laser power is 1 TW), the reflection efficiency still reaches 96.37%, confirming that TIR can be stably maintained within this high-efficiency regime. It is noted that for $a_0 = 0.087$ (Figure 4(c)), no detectable light intensity is observed behind the target, confirming that the laser energy is predominantly retained via TIR. In contrast, when $a_0 = 0.87$ (Figure 4(d)), a distinct transmitted signal emerges behind the target, demonstrating that a high-intensity laser can breach TIR constraints and penetrate the plasma target directly.

The physical origin of these transmission disparities lies in the dynamics of surface plasmon polaritons (SPPs). During TIR, surface waves propagate along the vacuum–plasma interface, inducing oscillating electric fields that generate surface charges. Collective oscillations of these charges form SPPs[39]. As the laser intensity increases, the electric field of the surface wave grows, amplifying electron oscillations and promoting the excitation of SPPs. Figure 5(a) demonstrates the synchronous evolution of plasma electron density perturbations (depicted by the red curve) and the electric field along the interface (represented by the blue curve), capturing the critical phase of laser–plasma interaction. The SPPs cause the electric field of the total-reflection-induced surface wave at the interface to be slightly lower than the theoretical value, as shown in Figure 5(b), where the amplitude of the electric field of the surface wave can be theoretically expressed as follows:

$$E_{\text{surf}} = \frac{2i\cos\theta_i\sqrt{n_p^2 - \sin^2\theta_i}}{n_p^2\cos\theta_i + i\sqrt{n_p^2 - \sin^2\theta_i}} \cdot \frac{m_e c\omega_0}{e} \cdot a_0. \tag{9}$$

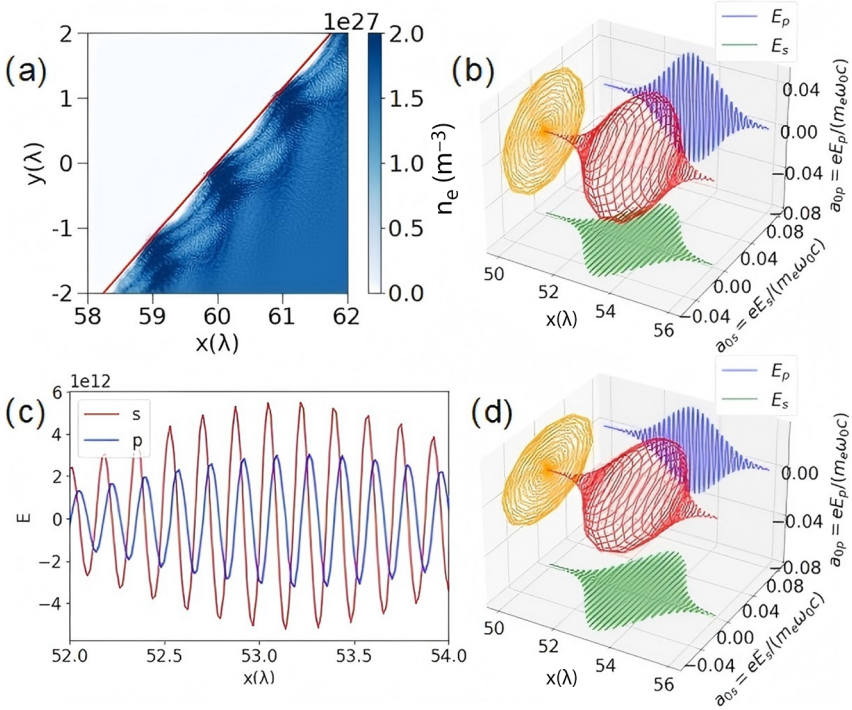


Figure 6. (a) Electron density distribution under the conditions of $a_0 = 0.87$ and $\lambda = 800$ nm. (b) Electric field intensity distribution along the central axis of the reflected laser when $a_0 = 0.087$ and $\lambda = 800$ nm. (c) Electric field of the reflected laser along the central axis, where the incident laser is set to linear polarization with a 60° angle in the y–z plane. (d) Three-dimensional state distribution diagram derived from the same dataset as in (c).

https://doi.org/10.1017/hpl.2025.10105 Published online by Cambridge University Press

Figures 5(c) and 5(d) show that plasma electron density responses vary significantly with a_0. At low amplitudes ($a_0 = 0.087$, Figure 5(c)), electron density perturbations remain minimal, and the interface remains smooth. At high amplitudes ($a_0 = 0.87$, Figure 5(d)), intense SPP excitation induces the formation of protrusive structures at the plasma–vacuum interface, accompanied by drastic electron density redistribution. These structures alter the laser incidence angle and plasma density gradient, allowing partial laser transmission around TIR conditions. Quantitatively, increasing a_0 from 0.087 to 0.87 decreases the reflection efficiency from 99.97% to 96.31%, directly validating the SPP-induced transmission enhancement. These findings deepen our understanding of laser–plasma interactions and offer insights for optimizing experiments where TIR efficiency matters.

4. Discussion

The plasma-based polarization modulator exhibits stable performance and can operate within a wide range of laser parameters. In principle, as long as the normalized parameter $\frac{n_e}{a_0 n_c}$ (the self-similar parameter in laser–plasma interactions) is fixed for different laser wavelengths, the present scheme can still be applicable[40,41]. That is, the mechanism presented here is also applicable to the optical laser pulse. To verify this point, we conduct additional simulations with the laser wavelength of 800 nm, while keeping the values of a_0 and $n_e = 0.9n_c$ the same as those for the case of the 36 nm wavelength laser.

Figure 6(a) shows that for the case of $a_0 = 0.87$, the resulting surface modulation on the plasma target is identical to that observed under the 36 nm wavelength condition, as shown in Figure 5(d). For the case of $a_0 = 0.087$, we investigate the polarization state of the reflected wave and find that the reflected wave remains CP, with the Stokes parameter P of 0.95 as shown in Figure 6(b). These results confirm that the present scheme can be well extended to lasers in the visible regime. While in these cases, the corresponding target is no longer a solid-density plasma but a near-critical-density plasma with density of 1.57×10^{21} cm^{-3}. Experimentally, carbon nanotube foam could be used to generate such near-critical-density plasma slab.

In the following, we shall further discuss some practical effects, including the polarization angle, the pre-plasma, the three-dimensional (3D) effect and the surface modulations. It is noted that in our simulations, the incident laser is actually set as 45° linear polarization in the y–z plane to ensure the conversion from linear polarization to perfect circular polarization. To demonstrate the influence of this polarization angle, we conduct an additional simulation with an initial 60° polarization angle relative to the y-axis in the y–z plane. As shown in Figures 6(c) and 6(d), the polarization state of the reflected light has changed. This is because the initial phases of the orthogonal polarization components of the incident light are equal, but their amplitudes are different. The TIR process only modifies the phase without altering the amplitude. Consequently, the phase difference of the reflected light still satisfies $\pi/2$, but the amplitudes remain unequal, resulting in elliptical polarization. Therefore, to achieve the conversion from linear polarization to

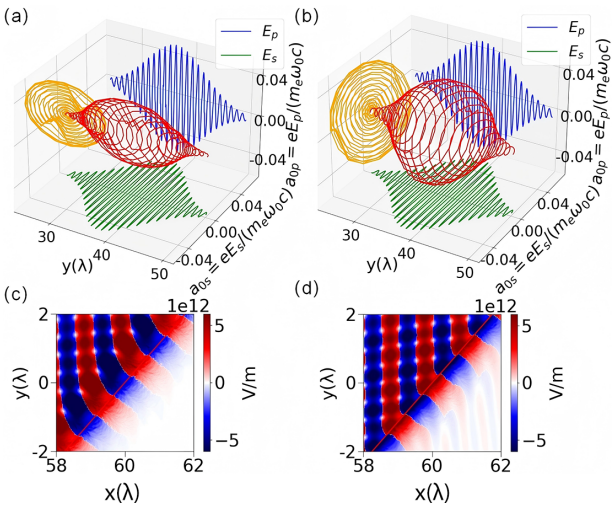


Figure 7. (a) Electric field of the reflected laser along the central axis at $b = 1$. (b) Electric field of the reflected laser along the central axis at $b = 5$. (c) Electric field distribution at the interaction moment when $b = 1$. (d) Electric field distribution at the interaction moment when $b = 5$.

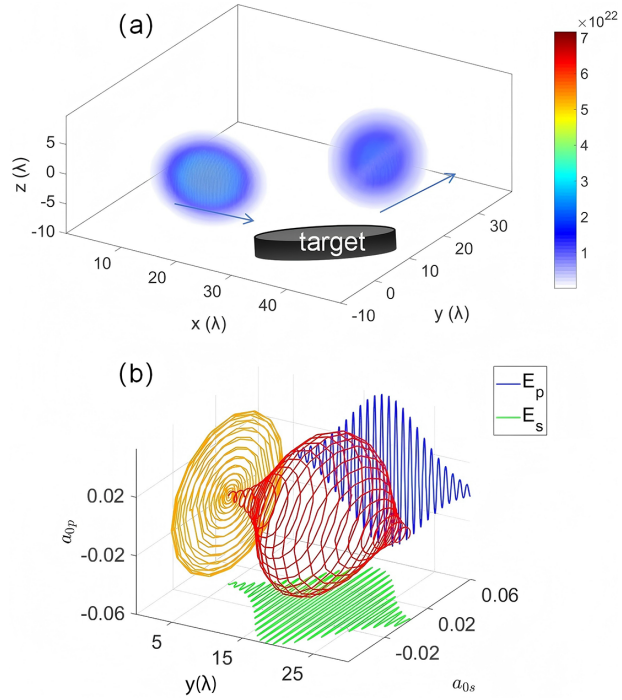


Figure 8. The 3D simulation results of (a) the spatial intensity distribution of the reflected laser and (b) the electric field intensity along the central axis of the reflected laser at $z = 0$.

https://doi.org/10.1017/hpl.2025.10105 Published online by Cambridge University Press

perfect circular polarization, the incident laser must be set to 45° linear polarization in the y–z plane.

Here we discuss the effects of pre-plasma. During the interaction between the laser and the plasma device, the laser usually produces pre-pulses (arriving at the target surface before the main pulse), which induce the formation of a pre-plasma layer that alters the electron density distribution near the target surface[42], thereby affecting TIR. Although the double-laser irradiation scheme[38] can lead to very homogeneous solid-density plasma, the existence of pre-plasma in front of the plasma surface is still inevitable. To simulate the impact of this process on polarization state conversion, an exponentially decaying pre-plasma was implemented ahead of the main plasma target, defined as follows:

$$n_e = n_{e0} \exp\left(-b\left(x - x_0\right)/\lambda_0\right), \tag{10}$$

where n_{e0} denotes the density of the main plasma target, λ_0 represents the wavelength of the incident laser and b governs the density decay rate (a smaller b corresponds to a larger-scale pre-plasma with a slower decay rate). Other parameters were kept unchanged during the simulation.

When $b = 1$ (corresponding to a relatively large-scale pre-plasma), as shown in Figure 7(a), the reflected laser exhibits elliptical polarization with Stokes parameter $P = -0.6 \pm 0.05$. This deviation arises from two factors: (1) refraction within the pre-plasma modifies the effective angle of incidence; (2) partial reflection in the pre-plasma layer disrupts the TIR process. As depicted in Figure 7(c), the incident laser interacts with the pre-plasma before contacting the plasma target, leading to an increase in the angle of incidence. In contrast, when $b = 5$, the influence is significantly reduced due to the thinner pre-plasma layer. As shown in Figure 7(b), the reflected laser remains CP with Stokes parameter $P = -0.94 \pm 0.04$. Figure 7(d) reveals that the angle of incidence of the laser remains almost unchanged in this case.

To improve the accuracy of the simulation, we further supplemented the study with a 3D geometric configuration. The simulation domain extends from 0 to $50\lambda_0$ in the x-direction, from $-10\lambda_0$ to $40\lambda_0$ in the y-direction and from $-10\lambda_0$ to $10\lambda_0$ in the z-direction. The simulation employs a 3D grid configuration with $800 \times 800 \times 320$ grid points. The grid spacing is $\lambda_0/16$, which is equivalent to 16 points per wavelength, and there are 10 particles per grid point. Parameters such as laser intensity, incident angle and plasma density remain unchanged, and the LP X-ray laser pulse has an incident angle of $\theta = 41.3°$.

As shown in Figure 8(a), the intensity distribution of the laser indicates that TIR has occurred, with almost no energy loss. Figure 8(b) shows the electric field amplitude of the reflected laser along the central axis at $z = 0$, confirming that its polarization state has been converted to left-handed circular polarization, with a Stokes parameter of $P = -0.96 \pm 0.04$. Therefore, this 3D simulation can also achieve efficient conversion from linear polarization to circular polarization.

In the practical case, surface modulation may also occur at the target surface on the X-ray wavelength scale. To describe this effect, we add a modulation function $R \times \sin(2 \times \pi \times y/\lambda)$ on the plasma surface to form a textured target, where R is set to 2, 5, 8 and 10 nm, respectively, as illustrated in Figure 9(a). In Figure 9(b), we present the s-polarized and p-polarized electric fields of the reflected

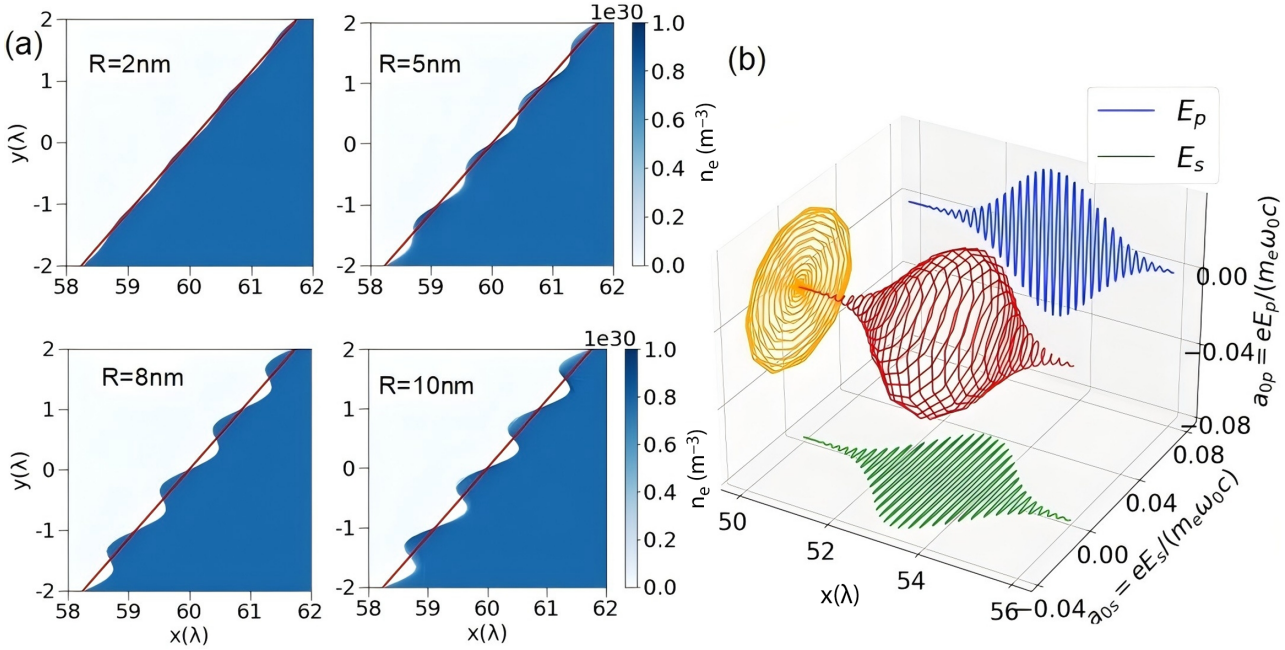


Figure 9. (a) Plasma density distribution of concave structures with a surface roughness of 2–10 nm. (b) Electric field intensity distribution along the central axis of the reflected laser ($R = 10$ nm).

https://doi.org/10.1017/hpl.2025.10105 Published online by Cambridge University Press

laser when $R = 10$ nm, and it is indicated that the polarization state remains circular. It is found that the influence of this modulated surface on the polarization state is negligible. However, as R increases, the total reflection efficiency decreases sequentially to 97%, 82%, 67%, 57% for $R = 2$, 5, 8 and 10 nm, respectively. This is attributed to the textured nature of the total reflection interface: some incident angles deviate from the designed value, and part of the laser undergoes direct transmission, leading to reduced reflectivity. It is noted that state-of-the-art nanofabrication techniques can already achieve a fabrication precision of 2 nm[43,44]. Therefore, the experimental realization of such an efficient polarization conversion regime could be feasible in the near-future.

5. Concluding remarks

We present a novel approach to achieve polarization conversion of high-power, high-intensity X-ray lasers via oblique reflection from a solid-density plasma target. Leveraging the refractive index of solid-density plasma (which is less than unity in the X-ray regime), TIR occurs when the X-ray laser is incident at angles exceeding the critical angle. This configuration enables compact and efficient polarization conversion. Particle-in-cell simulations confirm this plasma-based polarization modulator, demonstrating not only its high damage threshold and efficiency (up to 95% conversion efficiency) but also its tunability through adjustment of the incident angle. This combination of compactness, robustness, efficiency and adjustability positions the scheme as a versatile tool with potential applications in high-energy-density physics, advanced X-ray laser systems and related research frontiers.

Acknowledgements

This work is supported by the National Natural Science Foundation of China (Grant Nos. 12175154, 12475248, 12235014 and 12205201), the National Key R&D Program of China (Grant No. 2024YFA1613400), the Shenzhen Science and Technology Program (Grant No. RCYX20221008092851073), the Guangdong Province Key Construction Discipline Scientific Research Capacity Improvement Project (Grant No. 2021ZDJS107), the Guangdong Basic and Applied Basic Research Foundation (Grants Nos. 2025A1515010791 and 2025A1515012853) and the Natural Science Foundation of Top Talent of SZTU (Grants Nos. GDRC202310 and GDRC202423).

References

1. D. W. Brown, A. Losko, J. S. Carpenter, B. Clausen, J. C. Cooley, V. Livescu, P. Kenesei, J.-S. Park, T. J. Stockman, and M. Strantza, Metall. Mater. Trans. A **51**, 1379 (2020).
2. J. Epp, J. Dong, H. Meyer, and A. Bohlen, Scr. Mater. **177**, 27 (2020).
3. H.-H. König, N. H. Pettersson, A. Durga, S. Van Petegem, D. Grolimund, A. C. Chuang, Q. Guo, L. Chen, C. Oikonomou, F. Zhang, and G. Lindwall, Acta Mater. **246**, 118713 (2023).
4. A. C. de F. Silveira, R. Fechte-Heinen, and J. Epp, Addit. Manuf. **63**, 103408 (2023).
5. H. N. Chapman, P. Fromme, A. Barty, T. A. White, R. A. Kirian, A. Aquila, M. S. Hunter, J. Schulz, D. P. DePonte, U. Weierstall, R. B. Doak, F. R. N. C. Maia, A. V. Martin, I. Schlichting, L. Lomb, N. Coppola, R. L. Shoeman, S. W. Epp, R. Hartmann, D. Rolles, A. Rudenko, L. Foucar, N. Kimmel, G. Weidenspointner, P. Holl, M. Liang, M. Barthelmess, C. Caleman, S. Boutet, M. J. Bogan, J. Krzywinski, C. Bostedt, S. Bajt, L. Gumprecht, B. Rudek, B. Erk, C. Schmidt, A. Hömke, C. Reich, D. Pietschner, L. Strüder, G. Hauser, H. Gorke, J. Ullrich, S. Herrmann, G. Schaller, F. Schopper, H. Soltau, K.-U. Kühnel, M. Messerschmidt, J. D. Bozek, S. P. Hau-Riege, M. Frank, C. Y. Hampton, R. G. Sierra, D. Starodub, G. J. Williams, J. Hajdu, N. Timneanu, M. M. Seibert, J. Andreasson, A. Rocker, O. Jönsson, M. Svenda, S. Stern, K. Nass, R. Andritschke, C.-D. Schröter, F. Krasniqi, M. Bott, K. E. Schmidt, X. Wang, I. Grotjohann, J. M. Holton, T. R. M. Barends, R. Neutze, S. Marchesini, R. Fromme, S. Schorb, D. Rupp, M. Adolph, T. Gorkhover, I. Andersson, H. Hirsemann, G. Potdevin, H. Graafsma, B. Nilsson, and J. C. H. Spence, Nature **470**, 73 (2011).
6. A. Plech, M. Wulff, S. Bratos, F. Mirloup, R. Vuilleumier, F. Schotte, and P. A. Anfinrud, Phys. Rev. Lett. **92**, 125505 (2004).
7. J. O. Schunck, F. Döring, B. Rösner, J. Buck, R. Y. Engel, P. S. Miedema, S. K. Mahatha, M. Hoesch, A. Petraru, H. Kohlstedt, C. Schüssler-Langeheine, K. Rossnagel, C. David, and M. Beye, Optica **8**, 156 (2021).
8. T. Tajima, Eur. Phys. J. Spec. Top. **223**, 1037 (2014).
9. B. F. Shen, Z. G. Bu, J. C. Xu, T. J. Xu, L. L. Ji, R. X. Li, and Z. Z. Xu, Plasma Phys. Control. Fusion **60**, 044002 (2018).
10. J. Chakhalian, J. W. Freeland, G. Srajer, J. Strempfer, G. Khaliullin, J. C. Cezar, T. Charlton, R. Dalgliesh, C. Bernhard, G. Cristiani, H.-U. Habermeier, and B. Keimer, Nat. Phys. **2**, 244 (2006).
11. T. Funk, A. Deb, S. J. George, H. Wang, and S. P. Cramer, Coord. Chem. Rev. **249**, 3 (2005).
12. H. Ueda, M. García-Fernández, S. Agrestini, C. P. Romao, J. Van Den Brink, N. A. Spaldin, K.-J. Zhou, and U. Staub, Nature **618**, 946 (2023).
13. A. A. Lutman, J. P. MacArthur, M. Ilchen, A. O. Lindahl, J. Buck, R. N. Coffee, G. L. Dakovski, L. Dammann, Y. Ding, H. A. Dürr, L. Glaser, J. Grünert, G. Hartmann, N. Hartmann, D. Higley, K. Hirsch, Y. I. Levashov, A. Marinelli, T. Maxwell, A. Mitra, S. Moeller, T. Osipov, F. Peters, M. Planas, I. Shevchuk, W. F. Schlotter, F. Scholz, J. Seltmann, J. Viefhaus, P. Walter, Z. R. Wolf, Z. Huang, and H.-D. Nuhn, Nat. Photonics **10**, 468 (2016).
14. Z. F. Gao, H. X. Deng, B. Liu, and D. Wang, Chin. J. Lasers **47**, 0500015 (2020).
15. M. Suzuki, Y. Inubushi, M. Yabashi, and T. Ishikawa, J. Synchrotron Radiat. **21**, 466 (2014).
16. C. Emma, K. Fang, J. Wu, and C. Pellegrini, Phys. Rev. Accel. Beams **19**, 020705 (2016).
17. T. Tanaka, Phys. Rev. Lett. **110**, 084801 (2013).
18. E. Prat and S. Reiche, Phys. Rev. Lett. **114**, 244801 (2015).
19. X. R. Xu, Y. X. Zhang, H. Zhang, H. Y. Lu, W. M. Zhou, C. T. Zhou, B. Dromey, S. P. Zhu, M. Zepf, X. T. He, and B. Qiao, Optica **7**, 355 (2020).
20. P. Chen, T. W. Huang, K. Jiang, M. Y. Yu, and C. T. Zhou, Front. Phys. **10**, 1085045 (2022).

https://doi.org/10.1017/hpl.2025.10105 Published online by Cambridge University Press

21. P. Chen, T. W. Huang, K. Jiang, C. N. Wu, M. Y. Yu, and C. T. Zhou, Phys. Rev. Res. **5**, 013118 (2023).
22. J. Yamada, S. Matsuyama, I. Inoue, T. Osaka, T. Inoue, N. Nakamura, Y. Tanaka, Y. Inubushi, T. Yabuuchi, K. Tono, K. Tamasaku, H. Yumoto, T. Koyama, H. Ohashi, M. Yabashi, and K. Yamauchi, Nat. Photonics **18**, 685 (2024).
23. C. Thaury, F. Quéré, J.-P. Geindre, A. Levy, T. Ceccotti, P. Monot, M. Bougeard, F. Réau, P. d'Oliveira, P. Audebert, R. Marjoribanks, and P. Martin, Nat. Phys. **3**, 424 (2007).
24. R. Wilson, M. King, R. J. Gray, D. C. Carroll, R. J. Dance, C. Armstrong, S. J. Hawkes, R. J. Clarke, D. J. Robertson, D. Neely, and P. McKenna, Phys. Plasmas **23**, 033106 (2016).
25. Y. H. Kim, H. Kim, S. C. Park, Y. Kwon, K. Yeom, W. Cho, T. Kwon, H. Yun, J. H. Sung, S. K. Lee, T. T. Luu, C. H. Nam, and K. T. Kim, Nat. Commun. **14**, 2328 (2023).
26. O. Seemann, Y. Wan, S. Tata, E. Kroupp, and V. Malka, Nat. Commun. **14**, 3296 (2023).
27. H. Y. Wang, C. Lin, Z. M. Sheng, B. Liu, S. Zhao, Z. Y. Guo, Y. R. Lu, X. T. He, J. E. Chen, and X. Q. Yan, Phys. Rev. Lett. **107**, 265002 (2011).
28. L. L. Ji, J. Snyder, A. Pukhov, R. R. Freeman, and K. U. Akli, Sci. Rep. **6**, 23256 (2016).
29. S. Palaniyappan, B. M. Hegelich, H.-C. Wu, D. Jung, D. C. Gautier, L. Yin, B. J. Albright, R. P. Johnson, T. Shimada, S. Letzring, D. T. Offermann, J. Ren, C. Huang, R. Hörlein, B. Dromey, J. C. Fernandez, and R. C. Shah, Nat. Phys. **8**, 763 (2012).
30. R. Trines, F. Fiuza, R. Bingham, R. A. Fonseca, L. O. Silva, R. A. Cairns, and P. A. Norreys, Nat. Phys. **7**, 87 (2011).
31. Z. Y. Lei, Z. M. Sheng, S. M. Weng, M. Chen, and J. Zhang, Phys. Rev. Lett. **134**, 255001 (2025).
32. C. K. Carniglia and K. R. Brownstein, J. Opt. Soc. Am. **67**, 121 (1977).
33. X. Liu, Z. Chen, E. P. J. Parrott, B. S.-Y. Ung, J. Xu, and E. Pickwell-MacPherson, Adv. Opt. Mater. **5**, 1600697 (2017).
34. M. Milosevic, Appl. Spectrosc. **67**, 126 (2013).
35. J. D. Jackson, *Classical Electrodynamics* (John Wiley & Sons, 2012).
36. W. Kruer, *The Physics of Laser Plasma Interactions* (CRC Press, 2019).
37. T. D. Arber, K. Bennett, C. S. Brady, A. Lawrence-Douglas, M. G. Ramsay, N. J. Sircombe, P. Gillies, R. G. Evans, H. Schmitz, A. R. Bell, and C. P. Ridgers, Plasma Phys. Control. Fusion **57**, 113001 (2015).
38. N. F. Beier, H. Allison, P. Efthimion, K. A. Flippo, L. Gao, S. B. Hansen, K. Hill, R. Hollinger, M. Logantha, Y. Musthafa, R. Nedbailo, V. Senthilkumaran, R. Shepherd, V. N. Shlyaptsev, H. Song, S. Wang, F. Dollar, J. J. Rocca, and A. E. Hussein, Phys. Rev. Lett. **129**, 135001 (2022).
39. J. X. Zhang, L. D. Zhang, and W. Xu, J. Phys. D **45**, 113001 (2012).
40. A. Pukhov, Rep. Prog. Phys. **66**, 47 (2002).
41. T. W. Huang, A. P. L. Robinson, C. T. Zhou, B. Qiao, B. Liu, S. C. Ruan, X. T. He, and P. A. Norreys, Phys. Rev. E **93**, 063203 (2016).
42. C. R. Phipps, L. Zhigilei, P. Polynkin, T. Baumert, T. Sarnet, N. Bulgakova, W. Bohn, and J. Reif, J. Opt. Soc. Am. B **35**, LIM1 (2018).
43. C. Bostedt, S. Boutet, D. M. Fritz, Z. Huang, H. J. Lee, H. T. Lemke, A. Robert, W. F. Schlotter, J. J. Turner, and G. J. Williams, Rev. Mod. Phys. **88**, 015007 (2016).
44. J. Gour, S. Beer, P. Paul, A. Alberucci, M. Steinert, A. Szeghalmi, T. Siefke, U. Peschel, S. Nolte, and U. D. Zeitner, Nano **13**, 3645 (2024).

https://doi.org/10.1017/hpl.2025.10105 Published online by Cambridge University Press